DOI: 10.15587/978-617-8360-17-7.CH3

Oleksandr Shcheretskyi, Anatolii Verkhovliuk, Ruslan Sergiienko,
Dmytro Kanibolotsky, Volodymyr Shcheretskyi, Ievgenij Dzevin

3 PROSPECTIVE COMPOSITIONS OF HEAT-RESISTANT HIGH-ENTROPY ALLOYS FOR FOUNDRY PRODUCTION

ABSTRACT

The work investigates promising compositions of high-entropy alloys (HEAs) based on the FeNiCrCuAl and FeNiCrCuMn systems, which have the potential for use as heat-resistant materials in foundry production. It is shown that the use of a specially designed vacuum medium-frequency induction furnace allows obtaining high-quality ingots with active mixing of the melt and temperatures up to 1800°C. The thermodynamic parameters (entropy and enthalpy of mixing, atomic radii, electronegativities, VEC, Ω parameter) were calculated, on the basis of which the phase composition was predicted. X-ray phase analysis confirmed the formation of solid solutions with FCC and BCC lattices, an ordered B2 phase (of the NiAl type). In addition to phase analysis and structural study, the thermophysical properties (melting and crystallization heats, liquidus-solidus temperatures) of alloys, and elastic properties by the dynamic mechanical analysis (DMA) method, were investigated in a wide temperature range. The dependences of the elastic modulus and the loss factor on temperature were established. The heat resistance of alloys (at 900°C and 1000°C) was assessed, which showed high stability of the structure of high-entropy alloys in an oxidizing environment. The casting properties of the experimental alloys – fluidity and linear shrinkage – were studied using spiral and U-shaped test molds, which allowed comparing them with the indicators of cast irons and steels. The fluidity of high-entropy alloys of the FeNiCrCuMn system is lower, and that of alloys of the FeNiCrCuAl system is higher compared to standard steels (G25, GX10CrNiMn18-9-1). Thus, the results of the study confirm the feasibility of using alloys of the FeNiCrCuMn and FeNiCrCuAl systems as heat-resistant casting materials of a new generation.

KEYWORDS

High-entropy alloys, heat resistance, phase composition, elastic properties, thermophysical parameters, B2-phase, fluidity, induction melting.

In the early 2000s, a new type of materials was discovered – high-entropy alloys (HEAs) [1–3]. Traditional alloys have one or two main chemical elements, to which other elements are added in relatively low concentrations to achieve the desired properties. Whereas HEAs have at least five main elements, which are in an equiatomic or close to equiatomic composition. Due to the high concentration of components, such alloys have a high entropy of mixing, and it is entropy to a much greater extent than enthalpy that ensures the thermodynamic stability of HEAs. High-entropy alloys, due to the different diameters of the

atoms that make up their composition, have a deformed crystal lattice of the face-centered cubic (FCC) or body-centered cubic (BCC) types. Such alloys are characterized by unique properties: high values of the yield strength at room temperature, fracture toughness at low temperatures, resistance to softening at elevated temperatures, and wear resistance. High-entropy alloys with a BCC lattice are usually characterized by high hardness, while those with FCC lattice are characterized by high plasticity.

But conventional single-phase high-entropy alloys also have a number of disadvantages. Hard high-entropy alloys are brittle, while plastic ones have too low a yield strength. Conventional high-entropy alloys have poor casting properties: high volumetric and linear shrinkage and low fluidity. Also, individual components and the technology for producing high-entropy alloys are quite expensive. Usually, the method of arc remelting in a vacuum is used. These disadvantages limit the areas of practical use of high-entropy alloys.

One of the methods for improving the operational properties of HEAs is the manufacture of alloys with several high-entropy phases. This work is devoted to the development of cheap multiphase high-entropy alloys from available components with the prospects for mass casting production.

If the entropy of mixing ΔS_{mix} of the solution takes on large positive values, this leads to a significant negative contribution to the Gibbs free energy of mixing and stabilization of the corresponding solid phase. In the approximation of an ideal solution, the entropy of mixing ΔS_{mix} can be calculated as

$$\Delta S_{mix} = -R\sum_{i=1}^{N} c_i \ln(c_i), \tag{3.1}$$

where c_i – the mole fraction of component i in the melt, R – the universal gas constant.

In the case of equal molar concentrations c_i of each element, equation (3.1) takes the form

$$\Delta S_{mix} = R\ln n, \tag{3.2}$$

where n – the number of components in the alloy.

Alloys with an entropy of mixing greater than 12.5 J/mol K are considered high-entropy alloys [4].

The second thermodynamic function characterizing the stability of the phase is the alloy's enthalpy of mixing ΔH_{mix}, and its effect on the phase composition of the alloy is ambiguous. According to [5], the values of this function should be in the range –15 kJ/mol < ΔH_{mix} < 5 kJ/mol. At ΔH_{mix} > 5 kJ/mol, there is a lower degree of mixing of the components, which leads to segregation of elements in the alloy, and at high positive values of the enthalpy of mixing, stratification is possible. At high negative enthalpy of mixing ΔH_{mix} < –15 kJ/mol, the formation of intermetallics and ordered phases during melt crystallization is possible [6]. Only zero or small values of the enthalpy of mixing contribute to the random distribution of atoms in the crystal lattice sites and the formation of a disordered solid solution [7]. The enthalpy of mixing of a disordered multicomponent single-phase alloy is calculated by the equation [8, 9]

$$\Delta H_{mix} = \sum_{i=1;j\neq i}^{N} 4\Delta H_{ij}^{mix} c_i c_j, \tag{3.3}$$

where ΔH_{ij}^{mix} – enthalpy of mixing of a binary equiatomic alloy of components i and j; c_i, c_j – molar fractions of components in the corresponding multicomponent alloy.

The values ΔH_{ij}^{mix} calculated by the Miedema model for atomic pairs between elements with atomic numbers from 1 to 94 are presented in works [10–12].

The entropy of mixing is not always the dominant factor that ensures the formation of a single-phase structure and affects the microstructure. In work [13], the structures of HEAs were analyzed and three principles of the formation of solid solutions were formulated:

1) to obtain a high entropy of mixing, it is necessary that the number of main constituent elements be at least five;

2) the maximum difference in the atomic radii of the elements should not exceed 12%;

3) the enthalpy of mixing should vary in the range –40 kJ/mol < ΔH_{mix} < 10 kJ/mol.

In [5, 14], more precise parameters have been established, namely the coefficients Ω and δ_r, which can be used to predict phase formation in high-entropy alloys. The thermodynamic parameter Ω considers the influence of entropy and enthalpy of mixing, as well as the melting point on the formation of a solid solution [15]:

$$\Omega = \frac{T_m \Delta S_{mix}}{\left|\Delta H_{mix}\right|}, \tag{3.4}$$

$$T_m = \sum_{i=1}^{n} c_i \left(T_m\right)_i, \tag{3.5}$$

where T_m – the average melting point of an n-element alloy, K; $(T_m)_i$ – the melting point of the i-th element.

To describe the influence of differences in the atomic radii of the constituent elements, the empirical parameter δ_r can be expressed as follows:

$$\delta_r = \sqrt{\sum_{i=1}^{n} c_i \left(1 - \frac{r_i}{\bar{r}}\right)^2}, \tag{3.6}$$

$$\bar{r} = \sum_{i=1}^{n} c_i r_i, \tag{3.7}$$

where r_i – the atomic radius of the i-th component, $\bar{r}$ – the average atomic radius (taking into account atomic fractions).

A large difference in the atomic radii of the elements significantly affects the formation of a solid solution. Strong lattice distortions lead to an increase in the strain energy, and therefore to an increase in the free energy, which is accompanied by a decrease in the probability of solid solution formation, so the difference in the atomic radii of the elements should not exceed 6.6%.

Thus, the parameters Ω and δ_r can be a fairly reliable tool for separating between the formation of solid solutions and intermetallic phases in multicomponent systems. At a high value of the parameter Ω > 1.1 and a small value of the parameter $\delta_r \leq 4.6\%$ according to [5] or $\delta_r \leq 6.6\%$ according to [14], a solid solution based on phases with FCC or BCC lattice will form in the structure of the high-entropy alloy.

Based on the analysis of the structures of high-entropy systems, it can be stated that the formation of a solid solution is likely at the following values of the parameters mentioned above: $\Omega > 1.1$ and $\delta_r \leq 6.6\%$.

To describe the collective behavior of components in high-entropy alloys, the authors of [16, 17] proposed two additional parameters: the electronegativity difference ($\Delta\chi$) and the valence electron concentration (VEC). The value of $\Delta\chi$ is determined according to the classical Hume-Rothery rule:

$$\Delta\chi = \sqrt{\sum_{i=1}^{n} c_i \left(\chi_i - \overline{\chi}\right)^2}, \tag{3.8}$$

where χ_i – the Pauling electronegativity for the *i*-th element:

$$\overline{\chi} = \sum_{i=1}^{n} c_i \chi_i. \tag{3.9}$$

The current literature does not provide ranges of $\Delta\chi$ values that would indicate the formation of solid solutions in the HEAs structure, however, the study [18] showed that with a large value of $\Delta\chi$, the formation of intermetallic compounds or an amorphous phase is more likely. Judging from the tabular data [16, 18] and the relationship between the enthalpy of mixing and electronegativity [17], it can be concluded that for the existence of disordered solid solutions in the structure of high-entropy alloys, the difference in electronegativity ($\Delta\chi$) should not exceed 0.12 (or $\Delta\chi \leq 12\%$).

According to the Hume-Rothery rule [19], the valence electron concentration (VEC) predicts the type of crystal lattice. The valence electron concentration can also be used to predict the formation of intermetallics [20]. VEC is determined from the following equation:

$$VEC = \sum_{i=1}^{n} c_i \left(VEC\right)_i, \tag{3.10}$$

where $(VEC)_i$ – VEC for the *i*-th element.

VEC is a key physical parameter that governs the tendency for the formation of FCC and BCC solid solutions, a high VEC value (> 8), the FCC phase is formed, in the interval 6.87 < VEC < 8, a mixed BCC + FCC structure is formed, and at a lower VEC value (< 6.87) – the BCC phase [17].

In [21], a simple and practical pseudo-binary method was proposed for the design of eutectic HEA using the VEC and ΔH_{mix} parameters. Using this strategy, a series of nanostructured eutectic HEAs consisting of an ordered body-centered cubic (B2) phase and a phase with FCC lattice were successfully developed. By adding aluminum to high-entropy basic systems ($CoCrFeNi_2$, $Co_2CrFeNi$, $CoCrFe_2Ni$) with a FCC lattice, eutectic high-entropy alloys were obtained. Their eutectic structure consists of a mixture of a solid solution with FCC structure and intermetallic compounds (FCC/IMC). All developed alloys demonstrated unique mechanical properties with a tensile strength above 1000 MPa and a total elongation of more than 10%. When developing eutectic HEAs with FCC/IMC structure, the FCC solid solution is selected according to the following criteria: -5 kJ/mol $< \Delta H_{mix} < 0$ kJ/mol and VEC ≥ 8.

High-entropy alloys constitute a new class of structural materials that demonstrate a unique combination of high strength, heat resistance, corrosion resistance and wear resistance even under extreme operating conditions. Due to their stable microstructure and stability at high temperatures, HEAs are promising for use in the aerospace and energy industries (in particular, in elements of gas turbine engines and nuclear reactors), in military equipment, cryogenic systems, the chemical industry, as well as in the production of tools and bioinert implants and wear-resistant coatings [22, 23]. On their basis, unique new generation composite materials with controllable properties for critical engineering applications can be created [24, 25]. Another promising direction is the new HEAs based on lightweight elements that combine high thermal stability of the structure and resistance to local overheating during the joining processes involving high-energy sources [26].

3.1 PREPARATION OF HIGH–ENTROPY ALLOYS

To smelt high-entropy alloys in an argon atmosphere, a specialized induction vacuum furnace was developed and fabricated. It was based on a shaft-type vacuum resistance furnace, and its schematic diagram is shown in **Fig. 3.1** [27]. The tungsten heater was replaced by an inductor powered by a thyristor converter with a power of 6 kW and a frequency of 20–22 kHz. Melting was performed in an alundum crucible placed inside a graphite cup. The wall thickness of the graphite cup was optimized to minimize electromagnetic shielding of the charge, thereby ensuring active stirring of the melt during the process. The furnace manufactured in this way provided intensive mixing of the melt and overheated the alloy to a temperature up to 1800°C. The following were used as charge materials: carbonyl iron of special purity TU 6-09-3000-78 (Fe ≥ 99.99% wt.); cathode nickel (Ni ≥ 99.99% wt.); flakes of electrolytic chromium, grade ERX1 and chromium grade X99 in the form of small pieces; metallic manganese grade Mn997 (99.7 wt.%); copper grade M1 (99.9 wt.%) (the foreign equivalent Cu-ETP (99.9 wt.%)), aluminum ingot grade A85 (99.85 wt.%) (the foreign equivalent ENAW-1085 (99.85 wt.%)); electrolytic cobalt grade K0 (Co ≥ 99.98% wt.). Also, as a source of iron, nickel and chromium, stainless steel of the grade 10H18N9L (the foreign equivalents GX10CrNiMn18-9-1, EN 10213) was used. The technology for obtaining samples was as follows: after loading components into a crucible with a total mass of no more than 1500 grams, the working chamber was evacuated (P = 2.10-2 Pa), then flushed 2 times with high-grade argon (99.993%) and the furnace was filled with it to an excess pressure of 15–20 kPa. When heated to 1000°C, the heating rate did not exceed 25°C/min, so as not to crack the alundum crucible. During melting, the excess pressure of argon in the chamber rose to 30–40 kPa. After melting and dissolving all elements, the alloy was overheated to a temperature of 1550–1600°C and held in a liquid state for at least 30 min. The total duration of melting, including heating and holding the alloy in its liquid state, was at least 90 minutes. After holding the alloy in a liquid state in a high-purity argon environment, it was cooled together with the furnace to room temperature. The high-entropy alloys obtained in this way were remelted once more in an argon environment, and after the melting was completed, the furnace lid was opened, and the melt was poured into molds using traditional sand-clay casting. The chemical composition of the experimental HEA samples was determined using an X-ray fluorescence express analyzer (XRF) "EXPERT 3L".

The chemical composition of the obtained alloys is shown in **Table 3.1**.

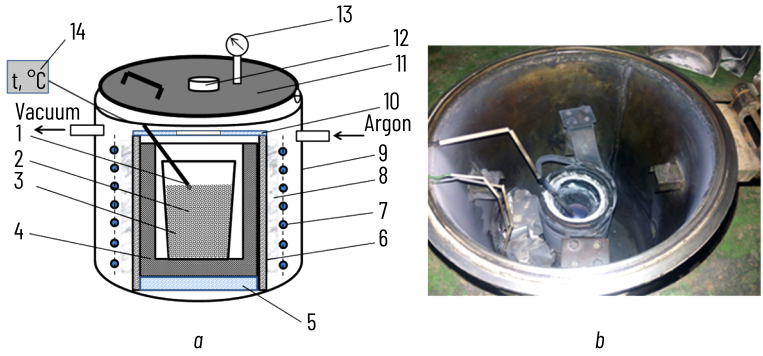

Fig. 3.1 Schematic diagram of vacuum induction furnace for smelting samples of high-entropy alloys: *a* – schematic diagram; *b* – photograph ; 1 – thermocouple; 2 – charge material; 3 – alundum crucible; 4 – graphite cup; 5 – alundum stand; 6 – alundum tube; 7 – inductor; 8 – kaolin wool; 9 – vacuum chamber; 10 – alundum cover with a viewing window; 11 – chamber cover; 12 – viewing window; 13 – vacuum gauge; 14 – temperature recording device

Table 3.1 Chemical composition of HEA samples, expressed in atomic percent

No.	Fe	Ni	Cr	Co	Mn	Cu	Al	C	Si	P+S
1	23.88	20.42	14.54	–	18.49	21.92	–	0.430	0.300	0.036
2	23.99	20.66	12.65	–	0.11	20.66	21.32	0.430	0.170	0.018
3	21.77	20.58	14.02	–	0.354	23.22	19.50	0.302	0.233	0.020
4	17.10	22.17	18.58	–	–	23.51	18.56	–	0.076	0.012
5	18.96	19.97	20.10	–	20.30	20.42	–	–	0.213	0.042
6	19.30	20.13	18.60	–	–	20.85	21.03	–	0.077	0.013
7	20.48	21.63	18.54	21.38	17.97	–	–	–	–	–
8	24.09	20.43	14.14	–	19.27	21.27	–	0.380	0.368	0.040
9	24.72	20.80	12.41	–	19.64	21.63	–	0.381	0.388	0.038
10	19.10	21.52	17.79	–	–	21.87	19.65	–	0.065	0.015

3.2 X–RAY PHASE ANALYSIS, MICROSTRUCTURE AND THERMODYNAMIC PARAMETERS OF HIGH–ENTROPY ALLOYS

X-ray phase analysis of the alloys was performed by X-ray diffraction on DRON-3, and Bruker D8 Advance diffractometer (Germany) using Mo-Kα (λ = 0.07093187 nm), Co-Kα (λ = 0.178897 nm) radiations, respectively, and with focusing of X-rays according to the Bragg-Brentano geometry. Depending on the type of radiation, measurements were carried out in the angular ranges of 10°—55° and 15°—135° with a step of 0.02° or 0.05°, respectively, with a pulse accumulation time of 2 s. For accurate determination of the lattice parameters in the region of far diffraction peaks at large angles, a step of 0.01° and an accumulation time of 12—16 s was used, depending on the type of sample. To study the microstructure and chemical phase composition of the HEA samples, a REM106I scanning electron microscope with an energy-dispersive microanalyzer (manufactured by OJSC "SELMI") was used. **Fig. 3.2** shows the diffraction patterns obtained on Samples No. 4 and No. 5 of the FeNiCrCuAl and FeNiCrCuMn systems, respectively. High-entropy alloys of the FeNiCrCuAl system demonstrate two phases with different crystal lattices, in particular BCC (the space group Pm3m) and FCC (the space group Fm3m). A solid solution based on the BCC phase has an ordered structure of type B2, which is characterized by a uniform distribution of all elements within the phase and exists in equiatomic NiAl alloys. The structure of type B2 is similar to a disordered solid solution based on a phase with a BCC structure of type A2 and differs in that the position in the center of the unit cell is occupied by one specific type of atoms, while another type occupies the corner positions. This is confirmed by the presence of a diffraction maximum (100) at $2\theta \approx 36°$ for Co-Kα radiation (**Fig. 3.2, *a***, Sample No. 4). The alloys of the FeNiCrCuMn system have a multiphase structure, but with different FCC lattices (FCC1, FCC2) with different periods and a BCC lattice (A2) (the space group Im3m) (**Fig. 3.2, *b***, Sample No. 5). The lattice periods were calculated for each reflection (*hkl*) in the X-ray diffraction pattern, and then the average value of the lattice parameters was determined. For certain X-ray diffraction patterns, Miller indices corresponding to large diffraction angles were selected to determine the lattice parameters. Specifically, the (321) peak from Sample No. 6 was observed at angles of 54.81° and 55.18°, using molybdenum radiation with wavelengths MoKα_1 = 0.7093187 Å and MoKα_2 = 0.710806 Å, respectively. The calculation of lattice parameters was also carried out on the basis of diffractograms using cobalt radiation (CoKα1 = 1.78897 Å). Lattice parameters depend on the chemical composition and for alloys of the FeNiCrCuAl system (Samples No. 3, 4, 6) the parameter of the BCC lattice varies from 2.8788 Å to 2.8900 Å, and the FCC lattice from 3.6358 Å to 3.6500 Å (**Table 3.2**). For alloys of the FeNiCrCuMn system (Samples No. 1, 5), the parameter of the FCC1 lattice changes from 3.6700 Å to 3.6800 Å, and the FCC2 lattice does not change at 3.6200 Å (**Table 3.2**). For alloys of the FeNiCrCuMn system, the diffraction pattern of one of the phases is similar to austenite or an iron-manganese alloy Fe_3Mn_7 with FCC1 lattice periods of 3.6700 Å, 3.6800 Å, respectively, and the second phase is similar to solid solutions in copper-iron alloys, but with slightly smaller parameters of the face-centered cubic FCC2 lattice (3.6200 Å). According to Vegard's law, the theoretical parameters of crystal lattices of alloys with the nominal charge composition $Fe_{20}Ni_{20}Cr_{20}Cu_{20}Al_{20}$ and $Fe_{20}Ni_{20}Cr_{20}Cu_{20}Mn_{20}$ were calculated. It turned out that they differ from the experimental ones, and the theoretical parameter of the BCC lattice has a larger value (2.9125 Å), and the parameters of the FCC lattice have smaller values (3.5039 Å, 3.6152 Å) compared to the experimental periods.

The discrepancy in the values of the experimentally determined and theoretically calculated parameters can be due to both the inaccuracy of the calculation and the change in the electronic structure, chemical composition, local order, magnetic and many other properties of solid solutions. In addition, the calculations did not take into account the influence of impurities of silicon, carbon, phosphorus and sulfur.

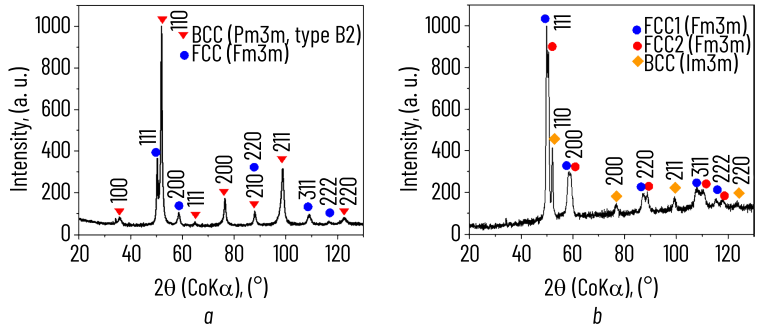

Fig. 3.2 X-ray diffraction patterns of high-entropy alloys: *a* — FeNiCrCuAl system (Sample No. 4); *b* — FeNiCrCuMn system (Sample No. 5)

Table 3.2 Results of phase analysis and lattice parameters of alloys of the FeNiCrCuAl, FeNiCrCuMn, FeCoNiCr systems

Sample	Lattice (space group)	Radiation	Lattice parameter, Å
1	**2**	**3**	**4**
Fe20Ni20Cr20Cu20Al20	BCC (Im3m) FCC (Fm3m)	calculation	2.9125 3.6152
Fe20Ni20Cr20Cu20Mn20	FCC (Fm3m)	calculation	3.5039
1	FCC 1 (Fm3m) FCC 2 (Fm3m)	CoKα	3.6800 3.6200
3	BCC (Pm3m) FCC (Fm3m)	CoKα	2.8800 3.6400
4	BCC (Pm3m) FCC (Fm3m)	CoKα	2.8900 3.6500
5	FCC 1 (Fm3m) FCC 2 (Fm3m) BCC (Im3m)	CoKα	3.6700 3.6200 2.8800

Continuation of Table 3.2

1	2	3	4
6	BCC (Im3m) BCC (Fm3m)	CoKα MoKα MoKα CoKα MoKα	2.8788±0.00460 2.8894±0.00536 2.8830* 3.6358±0.00517 3.6480±0.00510
FeNiCoCr	BCC (Fm3m)	CoKα MoKα	3.5702±0.00239 3.5768±0.0015**

*Note: The lattice parameters were calculated from peaks with Miller indices *(321), **(331) and (420).*

Typical microstructures of the cast high-entropy alloy samples of the FeNiCrCuAl and FeNiCrCuMn systems after crystallization are shown in **Fig. 3.3**. The cast samples exhibit a heterogeneous structure consisting of several phases, including dendrites, an interdendritic region, and a third phase enriched in copper. The branches of the dendrites have a rounded shape for both alloy systems. The chemical composition of the individual phases was determined using local chemical analysis (EDX analysis). In **Fig. 3.3, *a, b***, the structural components are indicated by numbers (1–7), and their corresponding chemical composition is presented in **Table 3.3**.

More refractory elements, such as iron and chromium, are concentrated in the branches of the dendrites, while the interdendritic regions are enriched in elements with lower melting points, such as copper, aluminum, manganese, and nickel. Unlike other alloy components, copper shows a tendency to segregation, forming a separate phase (**Fig. 3.3, *a***, point 4, **Fig. 3.3, *b***, point 7). This is due to its limited solubility in the FeNiCrAl-based solid solution and thermodynamic tendency to form copper-enriched regions, therefore, copper-enriched regions have a lower mixing entropy (**Table 3.3**). The calculated valence electron concentrations of individual phases indicate the potential formation of solid solutions with FCC or BCC lattices. In alloys of the FeNiCrCuAl system, the white elongated regions in the interdendritic space of alloy No. 4, enriched in copper (**Fig. 3.3, *a***, point 4), are characterized by the VEC equal to 9.566 el/at. This indicates the probable formation of a phase with FCC lattice. At the same time, the dendrites and the interdendritic space, where the VEC varies from 7 to 8 el/at (**Table 3.3**), probably contain a mixture of solid solutions with FCC and BCC lattices. This range of VEC corresponds to the transition zone between the stability of BCC and FCC phases, which indicates the possible coexistence of both types of crystal structures in the microstructure of the alloy. In alloys of the FeNiCrCuMn system, the dendrites have an elongated oval shape with uneven edges (**Fig. 3.3, *b***). The concentration of valence electrons suggests a high probability of forming two solid solutions in the interdendritic space of alloy No. 5, based on phases with a face-centered cubic lattice (**Table 3.3**, items 6 and 7). This is further supported by the results of X-ray phase analysis. The dendrites` branches of the alloy No. 5 of the FeNiCrCuMn system are enriched in chromium, therefore these regions are characterized by a lower mixing entropy compared to the interdendritic space (**Table 3.3**, point 5).

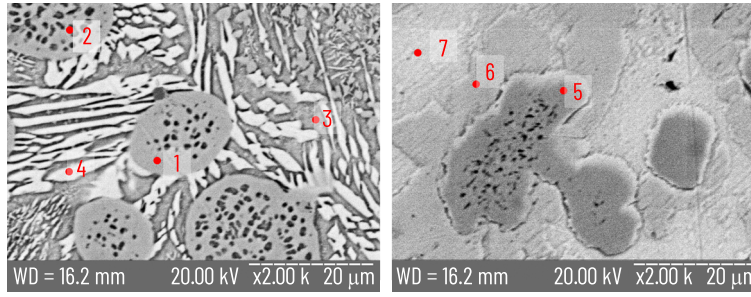

a *b*

Fig. 3.3 Microstructures of cast high-entropy alloys: a — No. 4 and b — No. 5 of the FeNiCrCuAl and FeNiCrCuMn systems. Individual phases are indicated by numbers, and their chemical composition is given in **Table 3.3**

Table 3.3 Chemical composition of individual phases in high-entropy alloys of the FeNiCrCuAl and FeNiCrCuMn systems

Alloy No.	Point	Chemical composition (at.%)						VEC (el/at)	ΔSmix (J/mol·K)	Lattice
		Fe	Ni	Cr	Cu	Al	Mn			
4	1	37.78	5.61	46.78	4.15	5.68	—	7.017	9.809	BCC FCC
	2	26.75	12.36	34.53	13.09	13.27	—	7.286	12.576	BCC FCC
	3	8.18	34.25	4.31	23.47	29.80	—	7.814	11.709	BCC FCC
	4	3.73	13.36	1.47	67.51	13.92	—	9.566	8.259	FCC
5	5	28.36	6.21	52.33	2.00	—	11.1	6.250	9.903	BCC
	6	25.31	25.39	19.99	10.01	—	19.3	8.215	13.016	FCC
	7	5.46	19.51	2.88	44.80	—	27.4	9.404	10.760	FCC

As shown in **Table 3.4**, the increased content of chromium and iron in the dendrites of alloys of both systems caused an increase in the microhardness of the dendritic branches, which turned out to be 1.1–2 times higher compared to the microhardness of the interdendritic regions. At the same time, in alloy No. 3, the opposite trend is observed — the interdendritic region demonstrates a slightly higher hardness.

Table 3.4 The microhardness of the structural constituents in FeNiCrCuAl and FeNiCrCuMn high-entropy alloy samples

Alloy No.	Microhardness, Hμ (kgf/mm²)		
	Interdendritic space	Dendrites	Shell around dendrites
1	233±39	233±32	–
2	198±20	296±58	–
3	328±51	290±52	–
4	245±24 263±57	322±41	–
5	194±25	288±41	330±44
6	343±42	375±60	–
8	172±13	192±37	–
10	195±17 252±28	381±42	–

To further evaluate phase formation and the development of solid solutions in the studied FeNiCrCuAl and FeNiCrCuMn alloys, key thermodynamic parameters were calculated, as summarized in **Table 3.5**. The concentration of valence electrons in the alloys of the FeNiCrCuMn system (Samples No. 1, 5, 8, 9) varied from 8.397 to 8.589 el/at, and for the alloys of the FeNiCrCuAl system (Samples No. 2–4, 6, 10) – from 7.601 to 7.846 el/at. These values indicate the formation of solid solutions with FCC lattice in the alloys of the FeNiCrCuMn system, and in the alloys of the FeNiCrCuAl system – a mixture of two phases with BCC and FCC lattices, which was previously confirmed by X-ray phase analysis. For the studied systems, the value of the thermodynamic parameter Ω exceeds 1.1. The alloys have relatively small negative values of the enthalpy of mixing ΔH_{mix} from –4.867 to –3.23 kJ/mol for the FeNiCrCuAl system and small positive values of ΔH_{mix} from 1.798 to 2.427 kJ/mol for the FeNiCrCuMn alloy system. All values of ΔH_{mix} are in the range –15 kJ/mol < ΔH_{mix} < 10 kJ/mol [5, 17, 28]. In addition, the configurational entropy coefficient $\Delta S_{mix}/R \geq 1.61$ also indicates the probability of solid solution formation (**Table 3.5**). A literature review of high-entropy systems shows that solid solution formation is likely when $\delta_r \leq 6.6\%$. The FeNiCrCuAl system exhibits an average atomic radius difference of ≤ 6.4%, influenced by the presence of aluminum (143 pm), while in the FeNiCrCuMn system it is about 4%. In the FeNiCrCuMn system, all elements have similar radii (from 124 to 130 pm), which contributes to a smaller δ_r and, accordingly, a higher probability of forming stable solid solutions. For reference, the atomic radii of elements in the studied systems are: Fe – 126 pm, Ni – 124 pm, Cr – 130 pm, Cu – 128 pm, Mn – 127 pm. The difference in electronegativity ($\Delta\chi$) has a minimal effect on the formation of a solid solution. Studies [16–18] show that at $\Delta\chi$ values exceeding 0.117, the formation of intermetallics is likely.

Table 3.5 Thermodynamic parameters of high-entropy alloys

Alloy No.	ΔSmix/R*	ΔSmix (J/mol·K)	ΔHmix (kJ/mol)	Ω	δr (%)	$\Delta\chi$	VEC	Lattice
1	1.635	13.597	1.992	11.50	4.091	0.147	8.56	FCC
2	1.628	13.538	–4.867	4.315	6.349	0.132	7.69	BCC+ FCC
3	1.644	13.669	–3.863	5.527	6.011	0.129	7.823	BCC+FCC
4	1.608	13.371	–3.230	6.587	5.461	0.125	7.846	BCC+FCC
5	1.624	13.504	2.427	9.549	3.256	0.143	8.397	FCC
6	1.615	13.424	–4.231	5.025	5.721	0.125	7.601	BCC+FCC
7	1.609	13.374	–4.153	5.814	3.171	0.136	8.033	FCC
8	1.636	13.601	1.799	12.74	4.046	0.148	8.540	FCC
9	1.628	13.535	1.798	12.62	4.066	0.148	8.589	FCC
10	1.612	13.404	–3.772	5.639	5.588	0.124	7.745	BCC+FCC

*Note: *R – universal gas constant (8.314463 J/mol·K).*

3.3 CASTING PROPERTIES OF HIGH-ENTROPY ALLOYS

To evaluate alloys as casting materials, their technological characteristics, which are commonly called casting properties, are studied. To date, the casting properties of high-entropy alloys remain insufficiently studied, which determines the relevance of the presented work. The main casting properties include fluidity, linear and volumetric shrinkage, crack resistance. In addition, this these characteristics include macro- and microstructure, the tendency of the alloy to gas saturation, contamination with oxide films during melting, as well as the manifestation of liquation heterogeneity of the composition. In this work, fluidity (λ) (the ability of the alloy to fill the cavity of the casting mold and accurately reproduce its configuration) and linear shrinkage (ε_l) were studied. To determine them, special test molds were developed that allow obtaining quantitative data: U-shaped cast iron test mold with a vertical channel, which is an improved modification of the Nehendzi–Samarin mold, and a sand-clay test mold with an annular channel [29]. For the manufacture of sand-clay test molds, quartz sand was used as a filler. Liquid glass (4–5% by mass), technical lignosulfonates and kaolin (2–3% by mass), as well as the special surfactant (mixture of sodium salts of alkylbenzenesulfonic acids), fuel oil (1–1.5% by mass) and technical urea were used as binders. To prevent the formation of burn-in on the surface of the castings during pouring, the inner surface of the sand-clay sample was covered with antipenetration paste, which included: marshalite (ground powdered quartz), polyvinyl butyral, technical alcohol, acetone and nitro enamel.

To ensure the feeding of the mold with liquid metal until complete solidification in the U-shaped channel, a sand-clay pouring cup (funnel) was used, which provided effective thermal insulation of the melt (**Fig. 3.4**). The dimensions of the pouring cup: external dimensions — diameter 90 mm, height 90 mm; cavity dimensions — diameter 50 mm, height 65 mm. The metal flowed from the cup into the cast-iron U-shaped sample through a transition channel 30–35 mm long and 13 mm in diameter, which ensured uniform metal flow from the funnel. This contributed to the initial stabilization of the filling rate of the cast iron mold, while the final stabilization was provided by the central downgate of the U-shaped mold itself. The temperature of the metal in the cast iron U-shaped test mold was controlled using a tungsten-rhenium thermocouple installed in the central riser near its junction with the U-shaped channel (**Fig. 3.4**, designation 3). Based on these measurements, the key thermal parameters of the experiment were determined: liquidus temperature, solidus temperature, cooling rate.

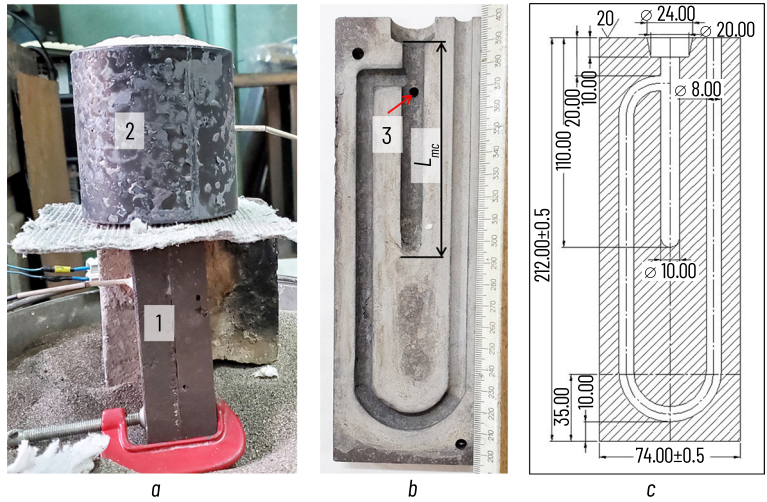

Fig. 3.4 Cast iron U-shaped test mold for determining fluidity and linear shrinkage of alloys according to the Nehendzi–Kuptsov method: *a* — photograph of the collected test mold; *b* — manufactured cast iron test mold; *c* — test mold`s drawing ; 1 — cast iron U-shaped test mold; 2 — sand-clay pouring cup (funnel); 3 — thermocouple installation location in the central downgate of the U-shaped test mold

The inner surface of the cast iron test mold was painted with a special water-based refractory paint (disthene-sillimanite — 70% by weight, perlite — 25%, bentonite — 2.5%, dextrin — 2.5%). Both halves of the mold after assembly were fixed with guide rods and a clamp. The temperature of the U-shaped mold was 16°C (room temperature). The pouring cup and the sand-clay mold with an annular channel, which was used as a test mold for fluidity, were dried at a temperature of 600°C for 3–4 hours.

After drying, the pouring cup was installed on the upper part of the U-shaped cast iron test mold, and the sand-clay test mold with an annular channel — on a special ceramic stand. One portion of molten metal weighing about 600 g was poured into the funnel of a U-shaped cast iron test mold, and the second portion of the same mass was poured into a sand-clay mold for fluidity test. The temperature of the melt before pouring was controlled in the furnace, then in the pouring cup and in both test molds (**Table 3.6**). The pouring time was 3–4 seconds.

Table 3.6 Pouring temperatures for fluidity and linear shrinkage of various alloys

Alloy	$t_{furnace}$, °C	$t_{pouring\ cup}$, °C	$t_{U\text{-}mold}$, °C	λ, mm	ε_l, %
FeNiCrCuMn	1450–1500	1400–1406	1180–1206	142–147 {65–105}	2.22–2.63
FeNiCrCuAl	1550–1600	–	–	320	2.50
G25 (AISI 1025)	1570	1514	1446	277{114}	1.95±0.15
GX10CrNiMn18-9-1 (AISI 304L)	1550	1459	1398	262{179}	2.66±0.058

*Note: In curly brackets is the length of the cost annular channel of the sand-clay mold (**Fig. 3.6**). $t_{furnace}$ — metal temperature in the crucible of the induction furnace before casting; $t_{pouring\ cup}$ — metal temperature in the pouring cup above the U-shaped test mold; $t_{U\text{-}mold}$ — metal temperature at the entrance to the U-shaped channel*

A control series of experiments were conducted to study the fluidity and linear shrinkage of high-entropy alloys of the FeNiCrCuMn and FeNiCrCuAl systems. For comparison, the casting properties of steel grades G25L (AISI 1025) and GX10CrNiMn18-9-1 (AISI 304L) were also determined.

As shown in **Fig. 3.5, 3.6** and **Table 3.6**, the fluidity of the FeNiCrCuMn high-entropy alloy is lower than that of standard steels, whereas the FeNiCrCuAl alloy exhibits higher fluidity. It is known that the fluidity of alloys is significantly affected by the chemical composition and other technological properties [30]. The increased fluidity of the FeNiCrCuAl system alloy can be explained by a shorter crystallization interval compared to the FeNiCrCuMn system alloy. In order to finally draw a conclusion about the fluidity of high-entropy alloys, it is necessary to conduct additional experiments: stabilize the metal pressure in the test mold, its geometric dimensions and configuration; control the temperature of the melt overheating above the liquidus temperature; and also control the temperature in the pouring cup.

It should also be taken into account that when using a massive metal U-shaped test mold, the influence of the thermophysical properties of the alloy under study on the result can be very significant. This influence increases with increasing heat transfer intensity from the metal to the mold. In this case, the thermophysical parameters of the alloy may become the predominant factor governing fluidity, diminishing the influence of other melt properties. No tendency to the formation of hot cracks was detected in the studied high-entropy alloys.

The linear shrinkage in this work was determined as the difference between the linear dimensions of the foundry mold cavity (L_{mc}) filled with molten metal and the dimensions of the resulting casting (L_c) after cooling, according to the formula [29]

$$\varepsilon_l = \frac{L_{mc} - L_c}{L_c} \cdot 100\%. \quad (3.11)$$

Prior to pouring the metal into the fluidity test mold, the linear dimension of the mold cavity (L_{mc}) was measured (**Fig. 3.4, *b***). After solidification, the length of the casting (L_c) formed in the central downgate of the U-shaped test mold was recorded (**Fig. 3.5**), and the linear shrinkage was subsequently calculated. The linear shrinkage of castings from high-entropy alloys of the FeNiCrCuMn and FeNiCrCuAl systems approaches the shrinkage of high-alloy steels and ranges from 2.22% to 2.63% (**Table 3.6**). The value of the linear shrinkage depends on the chemical composition of the alloy, the temperature and rate of filling the mold, as well as the cooling rate of the casting itself. It is known that the linear shrinkage of castings of gray cast iron is on average 1%, of steel — 2%, and for most other alloys — about 1.5%.

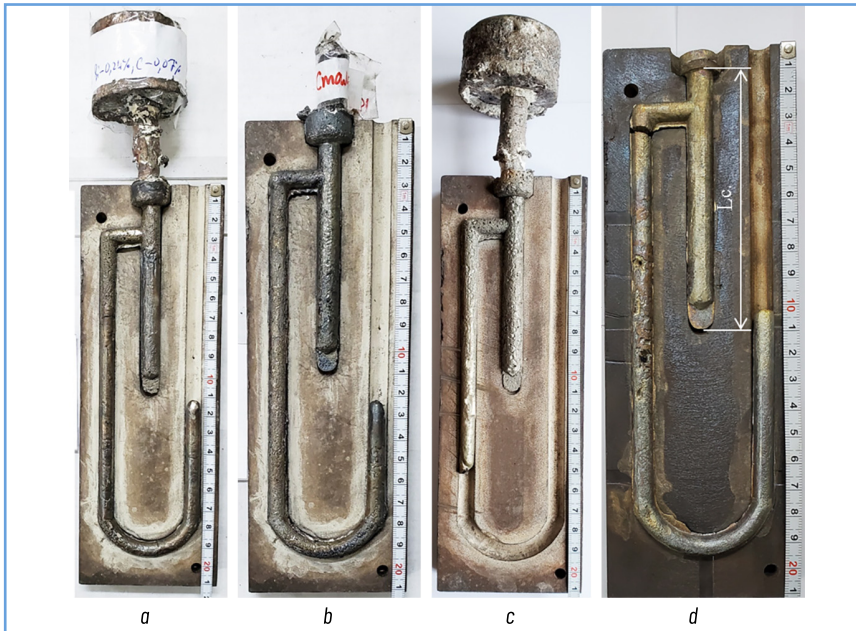

Fig. 3.5 Filled U-shaped channels in the Nehendzi–Kuptsov test mold with overfills for determining the fluidity of various alloys: *a* — casting from stainless steel GX10CrNiMn18-9-1 (λ = 262 mm); *b* — steel casting G25 (λ = 277 mm); *c* — high-entropy alloy casting of the FeNiCrCuMn system (λ = 142 mm); *d* — high-entropy alloy casting of the FeNiCrCuAl system (λ = 320 mm)

a *b*

c *d*

Fig. 3.6 Assembled complex sand-clay test mold and castings from various alloys for determining fluidity and mechanical properties: *a* — complex ring test mold; *b* — high-entropy alloy casting of the FeNiCrCuMn system (λ = 105 mm); *c* — stainless steel casting GX10CrNiMn18-9-1 (λ = 179 mm); *d* — gray cast iron (λ = 265 mm)

3.4 STUDY OF THE PHYSICAL AND MECHANICAL PROPERTIES OF HIGH-ENTROPY ALLOYS

Uniaxial tensile testing is relatively straightforward to analyze and enables the determination of several key mechanical properties of a material in a single test. These properties serve as quality indicators and are essential for engineering design calculations. Testing of samples with a diameter of 6 mm and a length of 30 mm was carried out on a tensile machine model P5.

Samples with a diameter of 3 mm and a length of 35 mm were stretched on a 1246P-2/2300 NIKIMP installation in accordance with the requirements of DSTU EN 10002-1:2006. The stretching rate was constant and was 1 mm/min, which corresponded to a deformation rate of $\dot{\varepsilon} = 10^{-3}$ s^{-1}. The load and elongation of the samples were measured using force and displacement sensors (extensometers) with adapters. During the tests, the yield strength ($\sigma_{0.2}$), the ultimate tensile strength (σ_u), relative elongation (δ), reduction of area (ψ) and the elastic modulus (E) were determined.

Brinell hardness was determined by applying a load of 750 kgf for 15 seconds using a hardened steel ball with a diameter of 5 mm pressed into the material. To determine the hardness by the Vickers method, a tetrahedral diamond pyramid with an angle at the apex of 136° was pressed into the samples. During the tests, loads of 10, 20 and 30 kgf were used; the holding time did not exceed 15 s.

The samples` hardness of alloys of the FeNiCrCuAl system (Samples No. 2–4, 6, 10) (**Table 3.7**) is more than one and a half times higher than the hardness of samples of the FeNiCrCuMn system (Samples No. 1, 5, 8, 9). The formation of a B2-ordered body-centered cubic (BCC) phase at higher aluminum contents is the main factor responsible for the hardness increase. In addition, a significant difference in the atomic radii of aluminum compared to other alloy elements causes local distortions of the crystal lattice, which additionally contributes to increasing hardness and temporary resistance to fracture. The results obtained are consistent with the data of other studies. In particular, in [31], experimental values of microhardness and reduced Young's modulus for the studied alloys in the entire range of aluminum concentrations are given. The dependence of microhardness is monotonic and reaches a maximum when the alloy consists entirely of a solid solution based on the BCC phase. Samples of the FeNiCrCuAl system with a mixed structure (with BCC and FCC lattices) in the cast state are characterized by brittle fracture in the elastic region: $\delta < 0.1\%$, $\psi < 0.1\%$, without a clearly defined conditional yield point (**Fig. 3.7**). In contrast, alloys of the FeNiCrCuMn system with FCC structure demonstrate high plasticity: $\delta = 40\%$, $\psi = 64\%$ (**Table 3.7**).

The ultimate strength or temporary fracture resistance (σ_u) was used in the formula [32]:

$$HB(HV) = k\sigma_u, \tag{3.12}$$

where the coefficient k is 2.54 for alloys of the FeNiCrCuMn system and 3.04 for alloys of the FeNiCrCuAl system were calculated.

Thus, high-entropy alloys with aluminum content are brittle, but are characterized by the highest hardness. In contrast, samples of the FeNiCrCuMn system with FCC structure have significant plasticity and relatively low hardness, while their ultimate tensile strength and yield strength are not inferior to those of high-alloy standard steels.

The tensile strength of alloys of the FeNiCrCuAl system exceeds the strength of high-strength cast iron of the EN-GJS-600-3 grade. Therefore, the mechanical properties of high-entropy alloys are determined by their crystal structure and elemental composition: alloys with a BCC lattice are characterized by high strength and low plasticity, while materials with FCC lattice, on the contrary, are characterized by lower strength but high plasticity.

Table 3.7 Hardness and mechanical properties of high-entropy alloys

Alloy No.	Hardness (kgf/mm²)		σ_u, MPa	$\sigma_{0.2}$, MPa	δ, %	ψ, %	Elastic modulus, GPa
	HB	HV					
1	156±13.5	–	603	335	40	64	122
2	309±6.4	–	997	–	–	–	–
3	228±36	246.4±10.5	735	–	–	–	136
4	304±25	–	981	–	–	–	–
5	218±18.5	–	842	–	–	–	–
6	291±8		939				
7	–	152±5.5	587	–	–	–	–
8	125±12	–	483	–	–	–	–
9	157±3.64	–	606	–	–	–	–
10	275±17.3	–	887	–	–	–	–

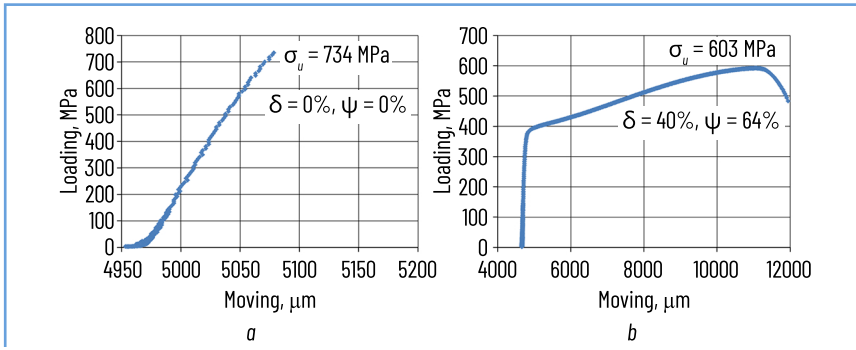

Fig. 3.7 Load-strain curves obtained during tensile testing of cast alloy samples belonging to the following systems: *a* — FeNiCrCuAl; *b* — FeNiCrCuMn

3.5 STUDY OF THE THERMOPHYSICAL CHARACTERISTICS OF THE OBTAINED ALLOYS

The thermophysical characteristics of the alloys were studied using a synchronous thermal analyzer (STA) of the STA 449F1 brand, manufactured by NETZSCH, Germany. STA is a combination of two research methods that are implemented simultaneously on one sample — thermogravimetry (TG) and differential scanning calorimetry (DSC). The main advantage of synchronous thermal analysis is that the mass change and thermal effects are measured on one sample simultaneously.

This approach provides a comparison of the results obtained by eliminating the influence of such factors as material heterogeneity, experimental conditions, sample preparation, etc. In addition, the combination of TG and DSC provides a more accurate determination of enthalpy values, since at any moment of the experiment the actual mass of the sample is known. In addition, the STA method saves time and sample material, which is especially important if the amount of the studied substance is limited, as well as when working with expensive or scarce materials.

The study of the thermophysical characteristics of the HEAs were carried out in crucibles made of alumina, in a dynamic environment of high-purity argon (20 ml/min). The heating and cooling rate was 20 K/min. The accuracy of temperature measurement was ±1°C. The sensitivity of the DSC signal registration was less than 1 μW. At the same time, the accuracy of determining enthalpy and heat capacity is ensured at the level of 3%. Thermal balances allow, during the experiment, to determine the current mass of the sample with an accuracy of 1×10^{-7} grams. The high sensitivity of the DSC allows to detect even insignificant thermal effects that arise in the material when heated or cooled, on the other hand, to record changes in the thermophysical properties of the sample under study. The ability of thermal balances to record the slightest change in the mass of the sample during the experiment allows to record the processes that occur in alloys during heating. Therefore, by the increase in the mass of the sample, it is possible to detect and control the oxidation of alloys. The loss of mass of the sample can be used to track the process of evaporation and decomposition. Therefore, synchronous thermal analysis is widely used in the study of high-entropy and amorphous alloys [33].

When studying the obtained high-entropy alloys, the melting point of the alloy (t_s — solidus temperature) was determined, and during cooling, the crystallization point (t_l — liquidus temperature) and the crystallization interval of the alloy were determined as the difference $\Delta t = t_s - t_l$. The alloy samples were heated to a temperature of 1450°C at a rate of 20 K/min, then cooled below 200°C and heated again to 1450°C (**Fig. 3.8**).

It is possible to distinguish the difference between the alloys of two different systems FeNiCuCrMn and FeNiCuCrAl during their melting (**Fig. 3.9**). The thermogram of the alloy containing manganese clearly shows two separate melting peaks from two different phases, while in alloys of the FeNiCuCrAl system containing aluminum, one broad asymmetric peak was usually recorded.

The results of the studies are given in **Table 3.8**.

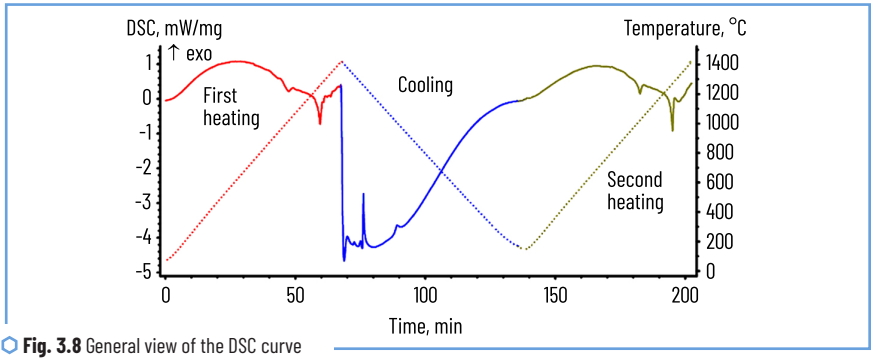

Fig. 3.8 General view of the DSC curve

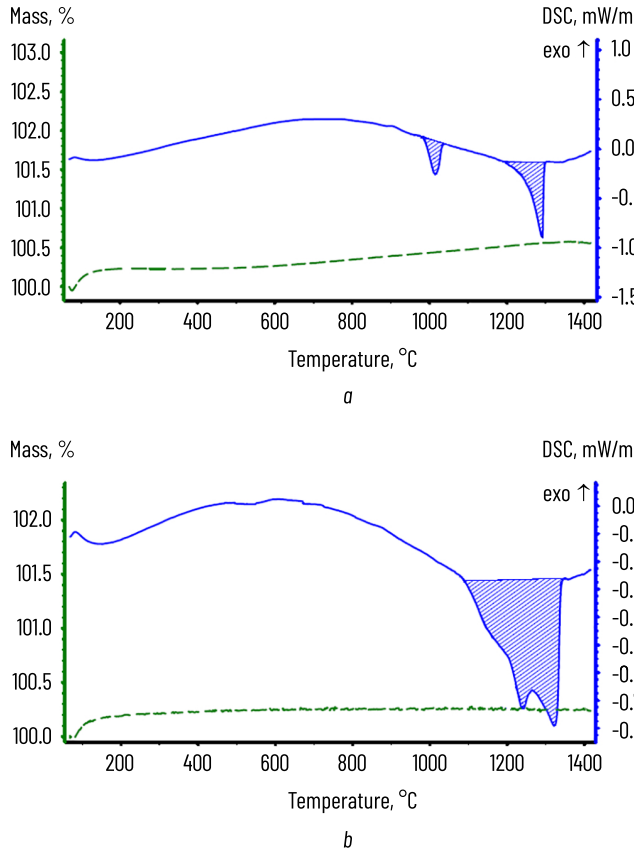

Fig. 3.9 STA curves: *a* — FeNiCrCuMn system; *b* — FeNiCrCuAl system

Table 3.8 Solidus, liquidus temperatures and crystallization intervals of high-entropy alloy samples

Sample No.	Solidus temperature, °C	Liquidus temperature, °C	Crystallization interval, °C	Melting heat, J/g	
				Solidus	Liquidus
1	2	3	4	5	6
1	988.6	1284.4	295.8	29	80
2	1200	1310.8	110.8	223*	–
3	1090	1320.8	230.8	226*	–

Continuation of Table 3.8

1	2	3	4	5	6
4	1123	1350	227	241*	–
5	996.9	1306.2	309.3	24	76
6	1098.5	1342.3	243.8	3,6	119
8	984.6	1281.2	296.6	30	131
9	990.8	1285.2	294.4	26	120
10	1100	1345.5	245.5	279*	

*Note: *Double peaks that cannot be separated.*

3.6 STUDY OF ELASTIC PROPERTIES OF HIGH–ENTROPY ALLOYS BY DMA METHOD

In this work, dynamic mechanical analysis (DMA) was first used to study the elastic properties and internal friction of high-entropy alloys depending on temperature. The basics of the DMA method were developed by K. Menard in 1998 [34]. DMA provides an opportunity to investigate the change in elastic properties of materials under the action of small periodic, usually sinusoidal dynamic loads depending on temperature, time and frequency. One of the leading companies in the world that produce DMA analyzers is the NETZSCH company (Germany). The DMA 242C analyzer of this company was used for the research.

Main technical characteristics of the DMA 242C analyzer of the NETZSCH company:

– temperature range: –170...600°C;

– frequency range: 0.01...100 Hz;

– range of adjustable loads: Max. ± 8 N static and Max. ± 8 N dynamic;

– range of deformation amplitudes: Max. ± 240 μm;

– sensitivity to the magnitude of deformation: 0.5 nm.

The appearance and schematic diagram of the DMA 242C analyzer are shown in **Fig. 3.10**.

As can be seen from the above characteristics, in this case very small loads are applied to the sample (total 1.6 kg), therefore this method is rarely used for metals and alloys. This method is widely used to study the mechanical characteristics of rubber, polymer films, polymers and fibers.

Based on the fact that the mechanical properties of alloys are structurally sensitive, that is, a change in the phase composition or structure of the material necessarily affects its mechanical characteristics, the DMA method was used not for its direct purpose – determining the absolute values of mechanical characteristics, but to study the features of structure formation in HEAs during their heat treatment and loading.

The principle of DMA operation is based on the registration of the reaction of the material (elongation, stress, phase shift, amplitude) to the action of small periodic dynamic loads depending on temperature, time and frequency. If a mechanical force (F) is applied to the sample under study, it will cause the

corresponding reaction of the material – deformation, stress, amplitude and phase shift. Registration of changes in parameters and appropriate mathematical processing make it possible to assess the influence of factors on the elastic properties of the material.

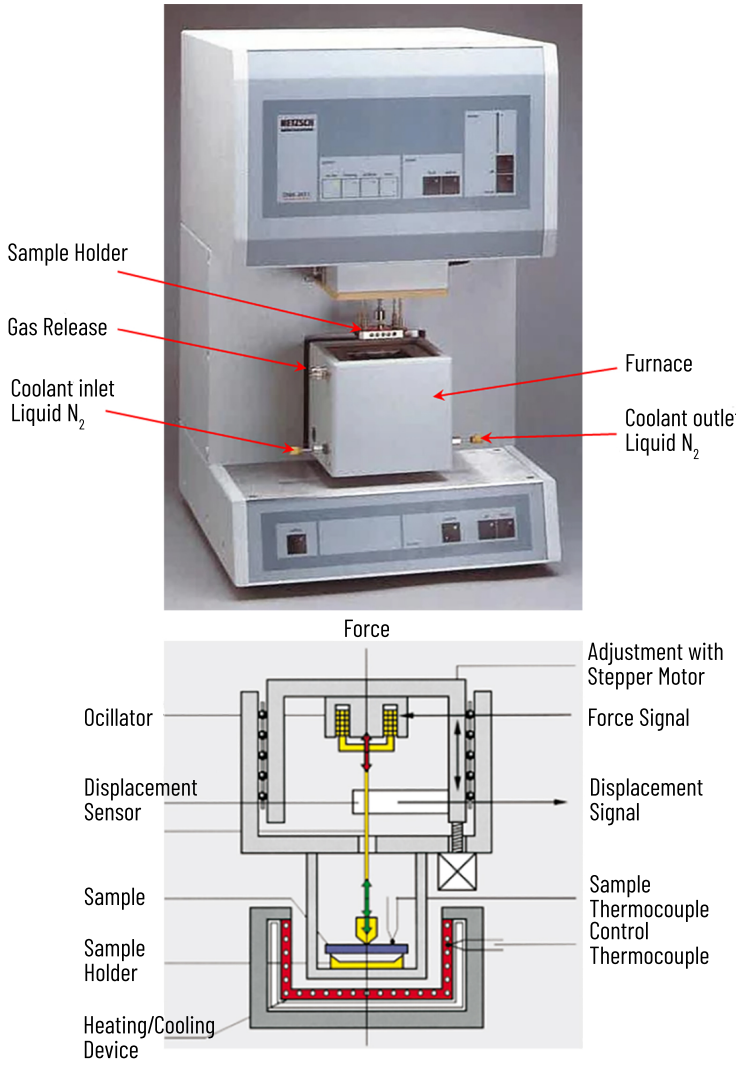

Fig. 3.10 Appearance and schematic diagram of the DMA 242C analyzer

As is known, the complex modulus of elasticity of a viscoelastic material can be written as:

$$|E| = \frac{\sigma}{\varepsilon}, \tag{3.13}$$

where E – the complex modulus, MPa; σ - the load, N; ε – the strain, μm; or

$$|E| = \sqrt{\left[E^{I}(\varepsilon)\right]^{2} + \left[E^{II}(\varepsilon)\right]^{2}}, \tag{3.14}$$

where E_I – the modulus of elasticity, characterizing the elastic properties of the material; E_{II} – the loss modulus, characterizing the conversion of mechanical energy into other types of energy, for example, into heat, and is a measure of the unreturned, lost energy of oscillations; ω – the frequency of oscillations.

Moduli of elasticity are vector quantities, the relationship between them is shown by the equations:

$$E^{I} = |E|\cos\delta, \tag{3.15}$$

$$E^{II} = |E|\sin\delta. \tag{3.16}$$

For an elastic material: $\alpha = 0$, cos 0 = 1, sin 0 = 0

$$E = E^{I}. \tag{3.17}$$

For a viscous material: $\alpha = 90^{\circ}$, $\cos 90^{\circ} = 0$, $\sin 90^{\circ} = 1$

$$E = E^{II}. \tag{3.18}$$

Often, to assess the elastic properties of materials, a quantity called the loss coefficient, or the tangent of the loss angle, or the internal friction of the viscoelastic system is used, it is defined as

$$\tan\alpha = \frac{E^{II}(\omega)}{E^{I}(\omega)}. \tag{3.19}$$

DMA analysis makes it possible to determine all the above parameters depending on time, temperature, load value and frequency. Additionally, it is possible to determine the coefficients of thermal expansion of the material.

DMA studies were carried out by the three-point bending method on samples measuring 2×1×45 mm at a static load of 8 N and a dynamic load of 7 N, a maximum amplitude of 100 μm and frequencies of 1, 5, 10 Hz.

Since there are no values of the elastic characteristics of high-entropy alloys in the literature, to assess the reliability of our results, a theoretical calculation of the elastic modulus was performed according to the additivity law:

$$E_{theor} = \sum_{i=1}^{n} c_i E_i, \tag{3.20}$$

where E_i – the Young's modulus of the i-th element; $c_i \leq 1$ – the concentration of the i-th element in atomic ratio; n – the number of elements in the alloy. The values of Young's modulus of pure metal elements are given in **Table 3.9**. The results of the studies are given in **Table 3.10** and **Fig. 3.11, 3.12**.

Table 3.9 Values of Young's modulus of pure metals

Metal	Al	Fe	Cr	Co	Ni	Mn	V	Ti	Zr	Nb	Hf	Ta
Young's modulus, GPa	70	210	250	200	200	194	135	120	97	105	137	186

Table 3.10 Elastic properties of the studied alloys

Alloy	Etheor, GPa	Eexp, GPa	Eexp/Etheor
$Ti_2ZrHfNbTa$	130.9	91	0.7
$TiZr_2HfNbTa$	134.2	119	0.88
$CrMnFeCo_2Ni_3$	210.7	194	0.92
$Al_5Cr_{15}Mn_{11}Fe_{18}Co_{17}Ni_{31}V_3$	202.9	147	0.72
$Al_{27}Cr_{16}Fe_{20}Co_{18}Ni_{19}$	174.9	131.2	0.75

Young's modulus and internal friction of the alloy are structurally sensitive parameters, therefore, using dynamic mechanical analysis, it is possible to establish those structural changes that are not recorded by DSC analysis, since they occur without thermal effects, or these effects are strongly stretched in time, therefore, DMA analysis can be used to study martensitic transformations [35, 36], relaxation in amorphous alloys [37] and other effects that are poorly recorded by other methods. The studies conducted in this way show that most of the obtained HEAs have structural transformations in the temperature range from 100 to 300°C.

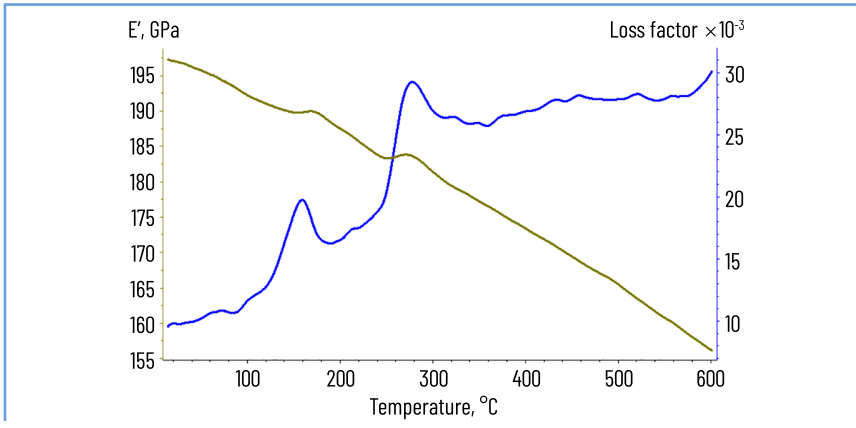

Fig. 3.11 Curves of dynamic mechanical analysis of high-entropy alloy $CrMnFeCo_2Ni_3$

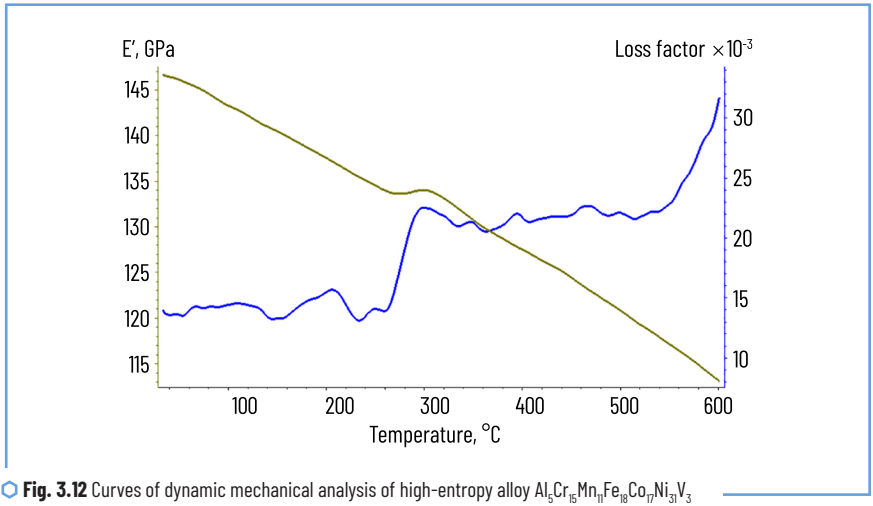

Fig. 3.12 Curves of dynamic mechanical analysis of high-entropy alloy $Al_5Cr_{15}Mn_{11}Fe_{18}Co_{17}Ni_{31}V_3$

3.7 RESEARCH ON THE HEAT RESISTANCE OF HIGH-ENTROPY ALLOYS

The heat resistance of high-entropy alloys was studied using the method of GOST 6130-71 "Methods for determining heat resistance", recording the ratio of the change in sample weight to its surface area (mg/cm^2). Using this method, the heat resistance of HEA samples that demonstrated low kinetics during heating and aging in an artificial air atmosphere at temperatures of 900°C or 1000°C was studied and the data were compared with standard alloys with different oxidation resistance.

To study the heat resistance, a STA 449 Jupiter F1 synchronous thermal analysis device was used. The study was carried out in an inert gas flow (high-purity argon 20 ml/min) and in a dynamic oxidizing environment (artificial air 20/80 O_2/N_2, 100 ml/min). The experiments were carried out on cast samples of the same size and shape. To establish the temperature and quantitative parameters of oxidation, two measurement modes were used: the study of oxidation kinetics and the study of heat resistance.

Mode 1. The samples were heated in air to 1450°C. The temperature of the onset of intensive oxidation was recorded using the thermogravimetry (TG) curve, which was determined by a sharp increase in the weight of the sample. The temperature of the onset of the exothermic effect and its enthalpy, which corresponds to the formation of an oxide film, were determined using the differential scanning calorimetry (DSC) curve. This mode allows to establish the characteristic temperatures of the onset of intensive oxidation with high accuracy (±1°C). The specific oxidation intensity was calculated as the ratio of the thermal effect to the surface area of the sample (J/g cm^2).

Mode 2. The samples were heated at the maximum possible rate of 50 K/min, subjected to isothermal holding in a stream of artificial air at 900°C and 1000°C for 4 hours with continuous control of the sample weight.

Heat resistance was estimated as the specific increase in the sample weight during the exposure time, related to its surface area (mg/cm^2.h).

Thermogravimetric diagrams of the oxidation of the samples were recorded and processed using the Netzsch Proteus software package.

There are compositions of the samples used for the studies in **Table 3.1**. In addition, Sample 7_1 was added to the study, which is close to Sample 7 but in its composition manganese was replaced by aluminum (actual composition in wt % of Al-15, Cr-17, Fe-23, Co-21, Ni-22).

For comparison of heat resistance, standard alloys G45, SM96, GX10CrNiMn18-9-1 were used. During the study, it was found that alloys G45, SM96 have low heat resistance compared to the studied samples of high-entropy alloys, therefore their values were not included in the final heat resistance comparison diagrams, these data can be found in **Table 3.11**.

Table 3.11 STA results of oxidation studies of standard alloys

No.	Alloy	Onset temperature of the intensive, oxidation °C	Oxidation intensity, J/g cm^2	Average oxidation at 900°C, mg/cm^2 h	Average oxidation at 1000°C, mg/cm^2 h
1	G45(C45)	948	2840	3.28	5.7
2	SM96	1113	358.3	0.85	2.31
3	GX10CrNiMn18-9-1	1142	1497	0.02	0.17

High-strength alloy SM96 with a special coating is used for the manufacture of blades of gas turbine engines, although it is excluded from the final comparison diagrams, it is heat-resistant, since compared to steel G45, its oxidation resistance is almost 4 times higher. Oxidation of this alloy occurs in two stages. The first stage begins at 1113°C and continues to 1318°C, in this temperature range there is moderate oxidation of the alloy, which leads to an increase in its weight by 0.63%. More intensive oxidation of this alloy begins at a temperature of 1318°C.

GX10CrNiMn18-9-1 steel showed sufficiently high heat resistance, therefore its results are shown in **Fig. 3.13** and **3.14** under number 8. Although this alloy has an temperature of intensive oxidation above 1000°C. Within prolonged exposure at 1000°C, its low oxidation intensity is initially maintained, but after 200 min exposure, the sample begins to oxidize intensively and the surface of the sample is quickly covered with a dense layer of oxide. After 30 minutes, an oxide layer forms on the surface of the sample, blocking access to the metal surface and the oxidation rate decreases, **Fig. 3.15**.

HEA Sample No. 1 when heated to 1000°C has a threshold for increasing the intensity of oxidation at a temperature close to 400°C and from this temperature gradually oxidizes (**Fig. 3.16**). Other HEA samples with manganese (Samples No. 5, 7) behave in a similar way. When exposed for 4 hours at 900°C, they continue to oxidize evenly, the intensity of oxidation decreases with exposure time, which is obviously a consequence of the oxide layer. But when heated to 1000°C, the intensity of oxidation remains approximately the same.

HEA No. 4 when heated to 1000°C practically does not oxidize during heating (**Fig. 3.17**). When exposed for 4 hours at 900°C, it oxidizes evenly with a very low intensity (average oxidation rate 0.001 mg/min). The same, low level of oxidation intensity is maintained when exposed at a temperature of 1000°C. HEA No. 6 behaves similarly, which is close in chemical composition to HEA No. 4 and contains Al at the base of its chemical composition.

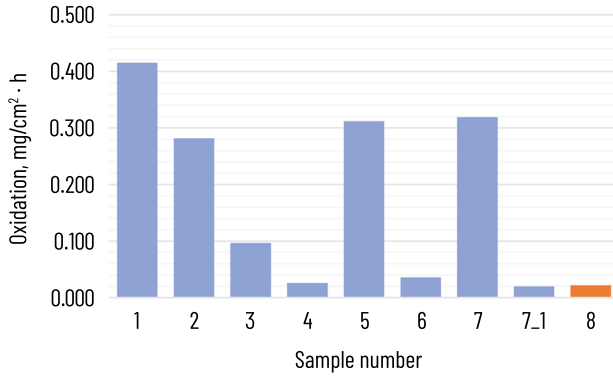

Fig. 3.13 Average oxidation of samples mg/cm²·h at 4-hour isothermal holding at 900°C

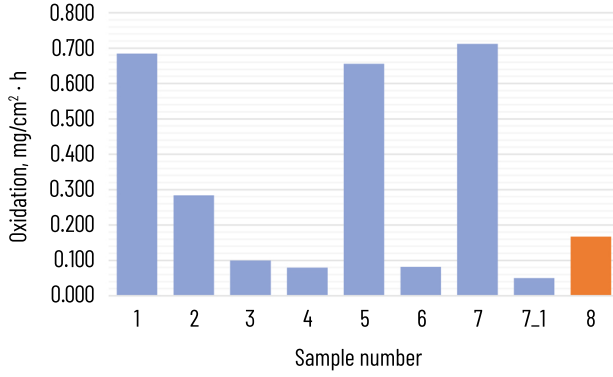

Fig. 3.14 Average oxidation of samples mg/cm²·h at 4-hour isothermal holding at 1000°C

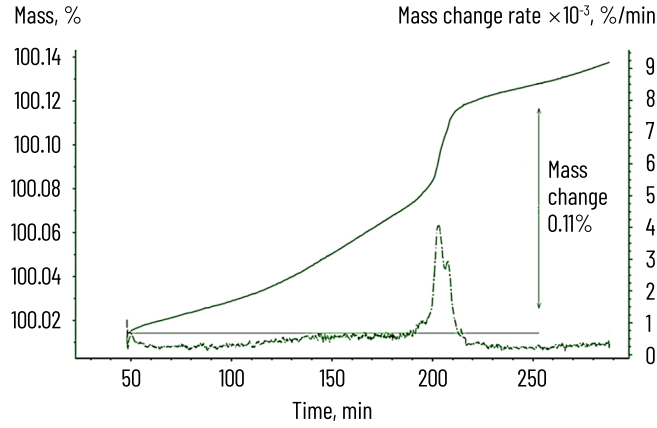

Fig. 3.15 Thermogravimetric diagram of steel GX10CrNiMn18-9-1 when exposed to artificial air at 1000°C

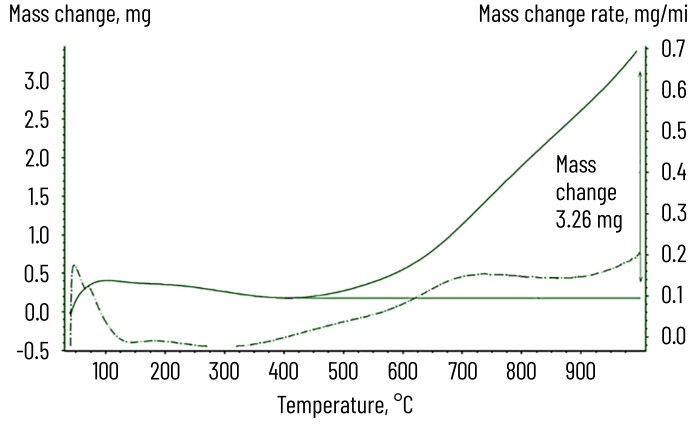

Fig. 3.16 Thermogravimetric diagram of the HEA Sample No.1 when heated to 1000°C

HEA Sample No. 3, similar in chemical composition, is oxidized more intensively, but still at a relatively low level. It demonstrates equally high heat resistance and its oxidation rate is in the range from 0.002 mg/min to 0.003 mg/min when exposed for 4 hours both at 900°C and at 1000°C.

HEA No. 2, when heated to 1000°C begins to gain weight of the oxide film at temperatures above 400°C, and already at a temperature of 516°C begins to oxidize intensively, rapidly gaining weight with an intensity of up to 0.219 mg/min (**Fig. 3.18**). The surface of the sample is quickly covered with a layer of oxide, which

blocks access to the metal surface and already at a temperature close to 800°C the oxidation rate decreases, but above 900°C the oxidation intensity begins to increase again.

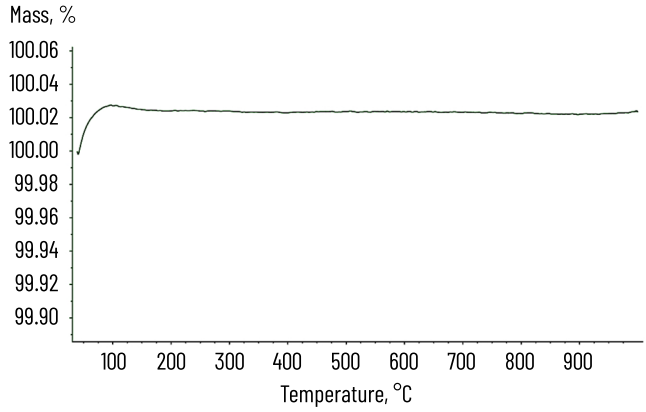

Fig. 3.17 Thermogravimetric diagram of HEA Sample No. 4 when heated to 1000°C

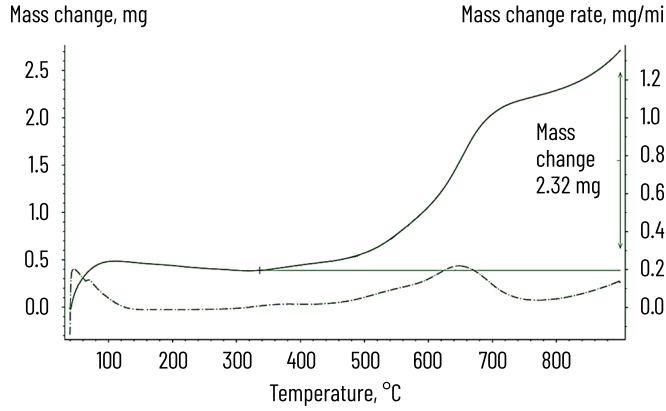

Fig. 3.18 Thermogravimetric diagram of the HEA Sample No. 2 when heated to 1000°C

After 4 hours at 900°C, the sample continues to oxidize evenly, but with a low oxidation intensity, since the oxide layer protects the surface of the sample. Approximately the same oxidation intensity is maintained after 4 hours at a temperature of 1000°C. Such a strong difference in heat resistance is probably directly related to the decrease in the chromium content in the sample.

A representative example is HEA Sample No. 7_1. Its composition is similar to that of HEA No. 7, but with manganese content replaced by aluminum. This substitution immediately altered the oxidation behavior. The heat resistance of this alloy at 900°C reaches the level of the reference alloy GX10CrNiMn18-9-1 (**Fig. 3.13**) and significantly surpasses it at 1000°C (**Fig. 3.14**). Furthermore, intensive oxidation is absent up to its melting point of approximately 1379°C.

HEA Samples No. 1, 5, 7 have average heat resistance, which significantly exceeds standard structural steels (G45) and even the heat-resistant alloy SM96. They begin to oxidize at 400—500°C, but the oxide layer at higher temperatures partially protects the materials.

HEAs samples No. 3, 4, 6, 7_1 practically do not oxidize at 900°C and 1000°C, surpassing steel GX10CrNiMn18-9-1 at temperatures above 900°C. Therefore, the oxidation behavior of the studied samples of high-entropy alloys differs depending on their composition. Thus, samples containing a combination of a significant amount of Al (6—11%) and Cr (14—18%), which contribute to the formation of protective oxide films Al203 and Cr203, have the best performance and an intensive oxidation temperature above 1000°C. Samples containing manganese and not containing aluminum have the lowest heat resistance in this alloy system. All samples with a high Mn content (~16—19%) showed the worst performance. HEA Sample No. 2 (Al ~11%, but Cr only ~13%) has worse resistance than HEA No. 3 (Al ~10%, Cr ~14%), which emphasizes the importance of the combination of these elements. The content of Copper (Cu) can worsen heat resistance, the most resistant samples are: No. 6 — has an average Cu content of ~20%, No. 7_1 does not contain copper at all (in its composition it is replaced by cobalt). HEA Sample No. 3 has the highest Cu content ~23.2%, which may also be the reason for the deterioration of heat and scale resistance indicators despite the presence of Al and Cr in sufficiently large quantities. This suggests that an excess amount of copper may be harmful and it is advisable to completely or partially replace it with cobalt to increase heat resistance.

CONCLUSIONS

A specially designed vacuum medium-frequency induction furnace provides reliable melting of high-entropy alloys (HEAs) at temperatures up to 1800°C with active mixing of the melt. This allows obtaining homogeneous ingots with precise chemical composition and minimizing the formation of non-metallic inclusions.

Thermodynamic analysis of HEAs compositions (estimation of mixing entropy, enthalpy, δ_r, $\Delta\chi$, VEC, Ω) showed that most of the studied alloys meet the criteria for the formation of solid solutions. In alloys with aluminum, the probability of the formation of ordered intermetallic phases of type B2 (NiAl) was revealed.

X-ray phase analysis confirmed the presence of FCC and BCC phases, in particular phases of type γ-Fe, B2-NiAl. In alloys with a high Mn content, two FCC phases with different lattice parameters are formed. The calculated lattice periods correlate with the theoretical VEC parameters.

Thermophysical characteristics of the alloys (liquidus/solidus temperatures, heats of fusion and crystallization) were determined experimentally based on STA studies. It was shown that the crystallization intervals for HEAs significantly affect their fluidity and dendritic morphology during casting.

The HEAs elastic properties were investigated by the method of dynamic mechanical analysis (DMA). It was found that the elastic modulus E' decreases with increasing temperature, and the loss tangent tgδ demonstrates stable viscoelastic behavior up to 600—700°C. This indicates good stability of the structure under thermomechanical loading.

The heat resistance of the alloys was tested at temperatures of 600—800°C. FeNiCrCuMn and FeNiCrCuAl alloys showed a slight change in mass, preservation of phase composition and microstructure, which indicates a high level of oxidative stability and suitability for long-term operation at high temperatures in air.

The casting properties of the HEAs (fluidity, shrinkage) were studied using spiral and U-shaped test molds. The best indicators were obtained for the the FeNiCrCuAl system alloys, which demonstrated a filling length of up to 320 mm, which exceeds the indicators of gray and special cast iron.

High-entropy alloys based on the FeNiCrCuAl system is promising heat-resistant casting material of a new generation. It combines good fluidity, high thermal stability, favorable microstructure and resistance to oxidation, which opens up wide possibilities for their practical application in critical machine components, heat exchangers, energy and chemical equipment.

FINANCING

The work was carried out within the framework of the program of Scientific and scientific-technical (experimental) works of the National Academy of Sciences of Ukraine in the priority area "Resource-saving, energy-saving and environmentally safe technologies of innovative materials for industry, medicine and defense" for 2025—2026, contract No. 5.9/25-П(1) dated 01.01.2025.

CONFLICT OF INTEREST

The authors declare that they have no conflict of interest in relation to this research, whether financial, personal, authorship or otherwise, that could affect the research and its results presented in this paper.

USE OF ARTIFICIAL INTELLIGENCE

The authors confirm that they did not use artificial intelligence technologies in creating the submitted work.

REFERENCES

1. Yeh, J.-W. (2002). U.S. Patent No. 2002/0159917 A1. High-entropy multielemental alloys. Available at: https://patents.google.com/patent/US20020159914A1/

2. Ranganathan, S. (2003) Alloyed pleasures: multimetallic cocktails. Current science, 85 (10), 1404—1406. Available at: https://www.currentscience.ac.in/Volumes/85/10/1404.pdf
3. Yeh, J.-W., Chen, S.-K., Lin, S.-J., Gan, J.-Y., Chin, T.-S., Shun, T.-T., Tsau, C.-H., & Chang, S.-Y. (2004). Nanostructured High-Entropy Alloys with Multiple Principal Elements: Novel Alloy Design Concepts and Outcomes. Advanced Engineering Materials, 6 (5), 299—303. https://doi.org/10.1002/adem.200300567
4. Miracle, D., Miller, J., Senkov, O., Woodward, C., Uchic, M., Tiley, J. (2014). Exploration and Development of High Entropy Alloys for Structural Applications. Entropy, 16 (1), 494—525. https://doi.org/10.3390/e16010494
5. Zhang, Y., Zhou, Y. J., Lin, J. P., Chen, G. L., Liaw, P. K. (2008). Solid-Solution Phase Formation Rules for Multi-component Alloys. Advanced Engineering Materials, 10 (6), 534—538. https://doi.org/10.1002/adem.200700240
6. Zhang, Y., Zuo, T. T., Tang, Z., Gao, M. C., Dahmen, K. A., Liaw, P. K., Lu, Z. P. (2014). Microstructures and properties of high-entropy alloys. Progress in Materials Science, 61, 1—93. https://doi.org/10.1016/j.pmatsci.2013.10.001
7. Zhang, Y., Lu, Z. P., Ma, S. G., Liaw, P. K., Tang, Z., Cheng, Y. Q., Gao, M. C. (2014). Guidelines in predicting phase formation of high-entropy alloys. MRS Communications, 4 (2), 57—62. https://doi.org/10.1557/mrc.2014.11
8. Miedema, A. R., de Châtel, P. F., de Boer, F. R. (1980). Cohesion in alloys — fundamentals of a semi-empirical model. Physica B+C, 100 (1), 1—28. https://doi.org/10.1016/0378-4363(80)90054-6
9. Niessen, A. K., de Boer, F. R., Boom, R., de Châtel, P. F., Mattens, W. C. M., Miedema, A. R. (1983). Model predictions for the enthalpy of formation of transition metal alloys II. Calphad, 7 (1), 51—70. https://doi.org/10.1016/0364-5916(83)90030-5
10. Takeuchi, A., Inoue, A. (2005). Classification of Bulk Metallic Glasses by Atomic Size Difference, Heat of Mixing and Period of Constituent Elements and Its Application to Characterization of the Main Alloying Element. Materials Transactions, 46 (12), 2817—2829. https://doi.org/10.2320/matertrans.46.2817
11. Boer, F. R. de, Mattens, W. C. M., Boom, R, Miedema, A. R., Niessen, A. K. (1998). Cohesion in metals. Transition metal alloys. Netherlands, 774.
12. Debski, A., Debski, R., Gasior, W. (2014). New Features of Entall Database: Comparison of Experimental and Model Formation Enthalpies. Archives of Metallurgy and Materials, 59 (4), 1337—1343. https://doi.org/10.2478/amm-2014-0228
13. Zhang, Y. (2010). Mechanical Properties and Structures of High Entropy Alloys and Bulk Metallic Glasses Composites. Materials Science Forum, 654-656, 1058—1061. https://doi.org/10.4028/www.scientific.net/msf.654-656.1058
14. Yang, X., Zhang, Y. (2012). Prediction of high-entropy stabilized solid-solution in multi-component alloys. Materials Chemistry and Physics, 132 (2-3), 233—238. https://doi.org/10.1016/j.matchemphys.2011.11.021
15. Yeh, J.-W.; Gao, M. C., Yeh, J.-W., Liaw, P. K., Zhang, Y. (Eds.) (2016). Overview of High-Entropy Alloys. High-Entropy Alloys. Springer International Publishing 1—19. https://doi.org/10.1007/978-3-319-27013-5_1
16. Guo, S., Liu, C. T. (2011). Phase stability in high entropy alloys: Formation of solid-solution phase or amorphous phase. Progress in Natural Science: Materials International, 21 (6), 433—446. https://doi.org/10.1016/s1002-0071(12)60080-x

17. Guo, S., Ng, C., Lu, J., Liu, C. T. (2011). Effect of valence electron concentration on stability of fcc or bcc phase in high entropy alloys. Journal of Applied Physics, 109 (10). https://doi.org/10.1063/1.3587228
18. Singh, A. K., Subramaniam, A. (2014). On the formation of disordered solid solutions in multi-component alloys. Journal of Alloys and Compounds, 587, 113–119. https://doi.org/10.1016/j.jallcom.2013.10.133
19. Jiang, L., Lu, Y. P., Jiang, H., Wang, T. M., Wei, B. N., Cao, Z. Q., Li, T. J. (2016). Formation rules of single phase solid solution in high entropy alloys. Materials Science and Technology, 32 (6), 588–592. https://doi.org/10.1179/1743284715y.0000000130
20. Zhu, J. H., Liaw, P. K., Liu, C. T. (1997). Effect of electron concentration on the phase stability of NbCr2-based Laves phase alloys. Materials Science and Engineering: A, 239-240, 260–264. https://doi.org/10.1016/s0921-5093(97)00590-x
21. Jin, X., Zhou, Y., Zhang, L., Du, X., Li, B. (2018). A new pseudo binary strategy to design eutectic high entropy alloys using mixing enthalpy and valence electron concentration. Materials & Design, 143, 49–55. https://doi.org/10.1016/j.matdes.2018.01.057
22. Li, H., He, W., Wang, F., Han, X., Wang, X., Wang, G. et al. (2024). Wear performance of FeCuMoTiV high entropy alloy coatings by laser cladding. Surface Topography: Metrology and Properties, 12(2), 025013. https://doi.org/10.1088/2051-672x/ad4403
23. Li, H., Shen, W., He, W., Jiao, L., Zhang, C., Song, Z. et al. (2025). Preparation of AlCoCrFeNi HEA wear-resistant coatings by laser cladding on the surface of (ZrB2+Al3Zr)/AA6016. Materials Today Communications, 48, 113575. https://doi.org/10.1016/j.mtcomm.2025.113575
24. Zhang, X., Li, H., Jiao, L., Wang, G., Wang, X., Zhang, C. et al. (2024). Effect of Rotational Speed on Microstructure and Properties of Al-Based Composite Reinforced with High-Entropy-Alloy Particles Fabricated by Friction Stir Processing. Advanced Engineering Materials, 26 (23). https://doi.org/10.1002/adem.202401417
25. Li, H., Li, C., Qiao, Y., Lu, S., Wang, F., Sun, C. et al. (2022). Preparation of in-situ ZrB2/A356 composites and high-temperature tribological studies. Materials Research Express, 9 (4), 046508. https://doi.org/10.1088/2053-1591/ac62b6
26. Korzhyk, V., Khaskin, V., Grynyuk, A., Peleshenko, S., Kvasnytskyi, V., Fialko, N. et al. (2022). Comparison of the features of the formation of joints of aluminum alloy 7075 (Al-Zn-Mg-Cu) by laser, microplasma, and laser-microplasma welding. Eastern-European Journal of Enterprise Technologies, 1 (12 (115)), 38–47. https://doi.org/10.15587/1729-4061.2022.253378
27. Shcheretskyi, O. A., Sergiienko, R. A., Verkhovliuk, A. M. (2022). Development and smelting of casting high-entropy alloys based on the Fe-Co-Ni-Mn-Cr system. Casting Processes, 148 (2), 50–59. https://doi.org/10.15407/plit2022.02.050
28. Yeh, J.-W. (2013). Alloy Design Strategies and Future Trends in High-Entropy Alloys. JOM, 65 (12), 1759–1771. https://doi.org/10.1007/s11837-013-0761-6
29. Verkhovliuk, A. M., Sergiienko, R. A., Shcheretskyi, O. A., Serhiiko, R. S., Potrukh, O. G., Kanibolotsky, D. S. et al. (2024). Casting properties of high-entropy alloys of the FeNiCrCuAl and FeNiCrCuMn systems. Casting Processes, 158 (4), 56–65. https://doi.org/10.15407/plit2024.04.056

30. Lakhnenko, V. L., Shcheretskyi, A. A., Apukhtin, V. V., Gavrilyuk, K. V. (2005). Methodological aspects of determining the fluidity of alloys with significantly different thermophysical characteristics. Casting Processes, 3, 28—34.
31. Kao, Y.-F., Chen, T.-J., Chen, S.-K., Yeh, J.-W. (2009). Microstructure and mechanical property of as-cast, -homogenized, and -deformed AlxCoCrFeNi (0≤x≤2) high-entropy alloys. Journal of Alloys and Compounds, 488 (1), 57—64. https://doi.org/10.1016/j.jallcom.2009.08.090
32. Pavlina, E. J., Van Tyne, C. J. (2008). Correlation of Yield Strength and Tensile Strength with Hardness for Steels. Journal of Materials Engineering and Performance, 17 (6), 888—893. https://doi.org/10.1007/s11665-008-9225-5
33. Shcheretskyi, O. A., Verkhovliuk, A. M., Sergiienko, R. A., Zadorozhnyy, V. Yu.; Fesenko, O., Yatsenko, L. (Eds.) (2021). Obtaining Nanostructured Materials by Heat Treatment of Amorphous Zirconium-Based Alloy. Nanooptics and Photonics, Nanochemistry and Nanobiotechnology, and Their Applications. Springer, 257—271. https://doi.org/10.1007/978-3-030-74800-5_17
34. Menard, K. P. (2008). Dynamic Mechanical Analysis: A Practical Introduction. CRC Press. https://doi.org/10.1201/9781420053135
35. Koval, Yu. M., Odnosum, V. V., Slipchenko, V. M., Filatova, V. S., Filatov, A. S., Shcheretskyi, O. A., Firstov, G. S. (2024). Influence of Grain Size on Shape Memory and Internal Friction in $Cu_{69.26}Al_{25.86}Mn_{4.88}$ Alloy. Metallofizika i Noveishie Tekhnologii, 46 (9), 933—941. https://doi.org/10.15407/mfint.46.09.0933
36. Ivanova, O., Shcheretsky, O., Podrezov, Y., Karpets, M. (2017). Young's modulus and damping capacity of Ti 3 Sn intermetallic compound with 1 at% and 3 at% of Zr and Al additions. Materials Science and Engineering: A, 683, 252—255. https://doi.org/10.1016/j.msea.2016.12.030
37. Sergiienko, R. A., Shcheretskyi, O. A., Zadorozhnyy, V. Yu., Verkhovliuk, A. M., Louzguine-Luzgin, D. V. (2019). Investigation of Zr55Cu30Al10Ni5 bulk amorphous alloy crystallization. Journal of Alloys and Compounds, 791, 477—482. https://doi.org/10.1016/j.jallcom.2019.03.270